European Journal of Cell Biology 101 (2022) 151273

Contents lists available at ScienceDirect

European Journal of Cell Biology

journal homepage: www.elsevier.com/locate/ejcb

Cell-substratum and cell-cell adhesion forces and single-cell mechanical properties in mono- and multilayer assemblies from robotic fluidic force microscopy

Ágoston G. Nagy [a,b], Inna Székács [b], Attila Bonyár [a], Robert Horvath [b,*]

[a] Department of Electronics Technology, Faculty of Electrical Engineering and Informatics, Budapest University of Technology and Economics, Budapest, Hungary
[b] Nanobiosensorics Laboratory, Institute of Technical Physics and Materials Science, Centre for Energy Research, Budapest, Hungary

ARTICLE INFO

Keywords:
Cell biomechanics
Cell adhesion
Forces
Fluidic force microscopy
Cell-cell forces

ABSTRACT

The epithelium covers, protects, and actively regulates various formations and cavities of the human body. During embryonic development the assembly of the epithelium is crucial to the organoid formation, and the invasion of the epithelium is an essential step in cancer metastasis. Live cell mechanical properties and associated forces presumably play an important role in these biological processes. However, the direct measurement of cellular forces in a precise and high-throughput manner is still challenging. We studied the cellular adhesion maturation of epithelial Vero monolayers by measuring single-cell force-spectra with high-throughput fluidic force microscopy (robotic FluidFM). Vero cells were grown on gelatin-covered plates in different seeding concentrations, and cell detachment forces were recorded from the single-cell state, through clustered island formation, to their complete assembly into a sparse and then into a tight monolayer. A methodology was proposed to separate cell-substratum and cell-cell adhesion force and energy (work of adhesion) contributions based on the recorded force-distance curves. For comparison, cancerous HeLa cells were also measured in the same settings. During Vero monolayer formation, a significantly strengthening adhesive tendency was found, showing the development of cell-cell contacts. Interestingly, this type of step-by-step maturation was absent in HeLa cells. The attachment of cancerous HeLa cells to the assembled epithelial monolayers was also measured, proposing a new high-throughput method to investigate the biomechanics of cancer cell invasion. We found that HeLa cells adhere significantly stronger to the tight Vero monolayer than cells of the same origin. Moreover, the mechanical characteristics of Vero monolayers upon cancerous HeLa cell influence were recorded and analyzed. All these results provide insight into the qualitative assessment of cell-substratum and cell-cell mechanical contacts in mono- and multilayered assemblies and demonstrate the robustness and speed of the robotic FluidFM technology to reveal biomechanical properties of live cell assemblies with statistical significances.

1. Introduction

Cellular monolayers have complex biology. They adhere to the extracellular matrix (ECM) via cell-matrix connections and form strong cell-cell contacts with neighboring cells, known as cell junctions (Knust, 2002). In mammals, the best example for such cellular organization is the endothelium, a special type of the epithelium, where a single cell layer barriers the blood or lymphatic circulation and the underlying tissue (Ricard et al., 2021; Claesson-welsh et al., 2021). In general, the epithelium covers vessels and cavities to distinguish tissues and organs from the surroundings (Torras et al., 2018; Vasquez et al., 2021). Acting as a barrier, the epithelium protects the body from extracellular damage while controlling its permeability regarding the transfer of substances, ions, and pathogens (Claesson-welsh et al., 2021; Torras et al., 2018; Bhat et al., 2019), and even controlling the expression of hormones (Haber et al., 2017). The polarity of epithelial cells also plays importance in their integration and assembly to a fully functional state during development and organoid formation, and the loss of polarity results in the epithelial-mesenchymal transformation (EMT) preceding cancer cell invasion of underlying tissues, the intravasation of the circulation and so metastasis formation (Knust, 2002; Friedl and Wolf, 2003; Friedl et al., 2012; Mierke, 2011; Clark and Vignjevic, 2015).

Epithelial cell-cell connections include various interacting protein complexes, such as desmosomes; gap junctions (GJs); adherens junctions

* Corresponding author.
E-mail address: horvath.robert@ek-cer.hu (R. Horvath).

https://doi.org/10.1016/j.ejcb.2022.151273

Available online 31 August 2022
0171-9335/© 2022 The Author(s). Published by Elsevier GmbH. This is an open access article under the CC BY-NC-ND license (http://creativecommons.org/licenses/by-nc-nd/4.0/).

(AJs) presenting E-cadherin, α- and β-catenin; tight junctions (TJs) including zona occludens proteins (ZO-1,2,3), claudin, occluding, etc. AJs and TJs are linked to the actin filament network of the cell, which influences the cells' migratory and regulatory behavior. At the multicellular level, cells render forces attributable to interactions with the ECM (traction force) and neighboring cells (intercellular force). Cell-cell junctions are stable mechanical connections between adjacent cells. Intercellular force transmission in epithelia is regulated via AJs, TJs, desmosomes, and the actomyosin network (Vasquez et al., 2017). Depending on the cell position, junctional force distributions fluctuate temporally and spatially in response to local variations in cell-matrix adhesions and cellular contractility (Ng et al., 2014; Mao and Baum, 2015). Also, TJs are heavily involved in inherited diseases, fighting off bacterial or viral infections, signaling, cell polarization, and expressing protein complexes mediating cell-cell adhesion (Knust, 2002; Bhat et al., 2019; Zihni et al., 2016). During development, the maturation of junctional assembly ensures functional consummation of cell-cell adhesion, initiated by the primordial junctions between two neighboring cells mediated by E-cadherin and nectin, which recruit the components of tight junctions (Zihni et al., 2016). Importantly, disruption of the TJs results in loss of function, where opportunist pathogens can enter the underlying tissue, or the regulation of active transport requiring processes is disturbed. During EMT, loss of E-cadherin leads to the destabilization of AJs, attended by increased cellular motility, invasiveness, and resistance to apoptosis (Onder et al., 2008). Whether the malfunction of the epithelial junctions and cell-cell adhesions is a cause or a result of cellular stress, such as cancer cell invasion, is still a question (Mierke and, 2008). During cancerous invasion, cancer cells express proteases, which disrupt the extracellular matrix and its contact to focal adhesions, and exhibit an increase in cell traction force and loss of intercellular forces. Focal adhesions play an essential role in cell-matrix adhesion, with special integrin-ligand connections anchoring the cells to the substrate, and their healthy function is critical in migratory, developmental, and cancer-related processes (Heintzman et al., 2009; Lock et al., 2018; Gerecsei et al., 2021; Peter et al., 2015; Kanyo et al., 2020).

Therefore, emphasizing the importance of epithelial connection maturation and the effect of cancer cell invasion on epithelial monolayers, we have studied the biomechanical properties of these connections with the robotized high-throughput nanofluidic force microscopy (robotic FluidFM) (Meister et al., 2009). The robotized FluidFM is a novel tool that facilitates high-throughput single-cell force-spectroscopy (SCFS), a widely acknowledged method to investigate cellular, bacterial or colloidal adhesion firmly attached to various surfaces (Nagy et al., 2020, 2019; Sztilkovics et al., 2020; Gerecsei et al., 2019; Benoit et al., 2000; Friedrichs et al., 2013; Sancho et al., 2017; Li et al., 2022; Guillaume-Gentil et al., 2014; Potthoff et al., 2015). The FluidFM technology enriches the method of fundamental atomic force-microscope (AFM) based SCFS recordings and enables reliable and fast recording of complete cell detachment processes due to the novel robotized platform. Of note, today, traditional AFM provides a higher signal-to-noise ratio and is ideal to measure molecular scale interaction events (Benoit et al., 2000; Friedrichs et al., 2013; Milles et al., 2018; Helenius et al., 2008). FluidFM is suitable to manipulate whole cells without the need of gluing the cells onto the AFM cantilever. In principle, the FluidFM applies hollow silicon-nitride cantilevers, which can be filled up with a liquid of our choice by a fluid reservoir connected to a pressure control system (Meister et al., 2009). This allows the disposition or suction of fluids in the femtoliter scale, providing exciting novel methodologies in the field of mechanobiology (Nagy et al., 2020, 2022a; Sztilkovics et al., 2020; Sancho et al., 2017), injection, extraction, or transplantation procedures on living cells (Guillaume-Gentil et al., 2017, 2016; Gäbelein et al., 2021), colloidal spectroscopy (Gerecsei et al., 2019; Sancho et al., 2017; Helfricht et al., 2017), 2D-3D microprinting (Saftics et al., 2019; Hirt et al., 2015, 2017; Pattison et al., 2022), and some newly introduced biophysical techniques (Li et al., 2022; Koehler et al., 2021; Aramesh et al., 2019; Chen et al., 2022). To access the strength and the force transmission of cells, focal ligand-receptor adhesions must be separated, for which the SCFS techniques are well suited. The FluidFM is able to perform such experiments by approaching a targeted cell with its buffer-filled cantilevers, and upon reaching the cell, suction is applied to attach the cell to the aperture at the end of the cantilever. After establishing contact, by retracting the cantilever, the targeted cell is detached from the substrate, and a characteristic force-distance (FD) curve can be measured, where the force is calculated based on Hooke's law commonly used in AFM applications, and the distance is the position of the cantilever measured from the starting point (see Fig. 1). From the characteristic FD-curve, biomechanical parameters can be obtained and analyzed, such as the maximal force of cell detachment (F_{max}), the traveled distance of the cantilever, with respect to the surface at F_{max} (D_{max}), and the integrated FD-curve area, known as adhesion energy (usually called as work of adhesion in AFM studies) (E_{max}). These parameters and their cell area normalized derivatives represent a cell's adhesive properties, and when measured for a large number of cells, can be used to assess population distributions and cell to cell differences.

In this work, we present a study on cell-substratum adhesion maturation of the epithelial Vero cell line, and as a contrast, cancerous HeLa cells were also tested under the same conditions, recorded with robotized FluidFM (see Fig. 1). As substratum, a thin gelatin layer was used in all cases, which promotes integrin αvβ3 and α5β1 connections to RGD-domains in the gelatin, and so provides an ideal basement membrane for focal adhesion (Davidenko et al., 2016; Kozyrina et al., 2020). In this manner, the differences between cell lines can be well described and quantified, and also the importance of healthy cell-cell contacts can be highlighted. A new methodology is introduced to quantify the cell-cell contact strength, based on experimental data recorded with FluidFM and phase holographic imaging (Peter et al., 2015; Nagy et al., 2022b), especially derived for epithelial cells like Vero, which form a confluent cuboidal monolayer. Vero cells are widely used in numerous laboratories for vaccine development and toxin screening, but because of contact inhibition, they maintain normal cell function and morphology, unlike cancer cells (Kiesslich and Kamen, 2020; Ammerman et al., 2008). HeLa is also one of the most commonly used cell lines, presenting an ideal model for studying immortal cancer cells. Therefore, both cell lines are well-known candidates for investigating cell-cell and cell-substrate contact development. To address the question of cell invasion, HeLa cells were seeded on top of the tight Vero monolayer to study their adhesion strength and effect on the monolayer itself. Similar approaches have already been performed in important AFM studies (Puech et al., 2006; Jaczewska et al., 2014) that measured initial contact formation. To address contact maturation here we present high-throughput SCFS data representing the attachment forces and detachment work (adhesion energy) of strongly adhered cells from the single-cell state to confluent layers. Such quantification of cell-cell adhesions is crucial in many aspects, such as cancer, fertility, and immunology research and development.

2. Results and discussion

The total number of cells investigated in our study is 214, of which 86 are HeLa and 128 are Vero cell, where all of the evaluated cells were fully detached from the substrate through rupture events. The categories and used abbreviations with the respective cell numbers are: single-cell with no neighboring cells picked up from the gelatin coating (SC; 19 HeLa, 18 Vero), cells picked up from island like cell assemblies (ISL; 19 HeLa, 19 Vero), single HeLa cells picked up from a confluent HeLa layer (HeLa CFL; 20 HeLa), Vero cells picked up from a sparse monolayer (ML) of Vero cells (sparse Vero ML; 20 Vero), Vero cells picked up from a tight Vero ML (26 Vero), HeLa or Vero cells picked up from the top of the tight Vero monolayer (HeLa TOP, Vero TOP; 25 HeLa, 16 Vero), and Vero cells picked up from a tight Vero ML when HeLa cells were present (with potential influence) on the top of the Vero layer (Vero ML-HeLa, 23

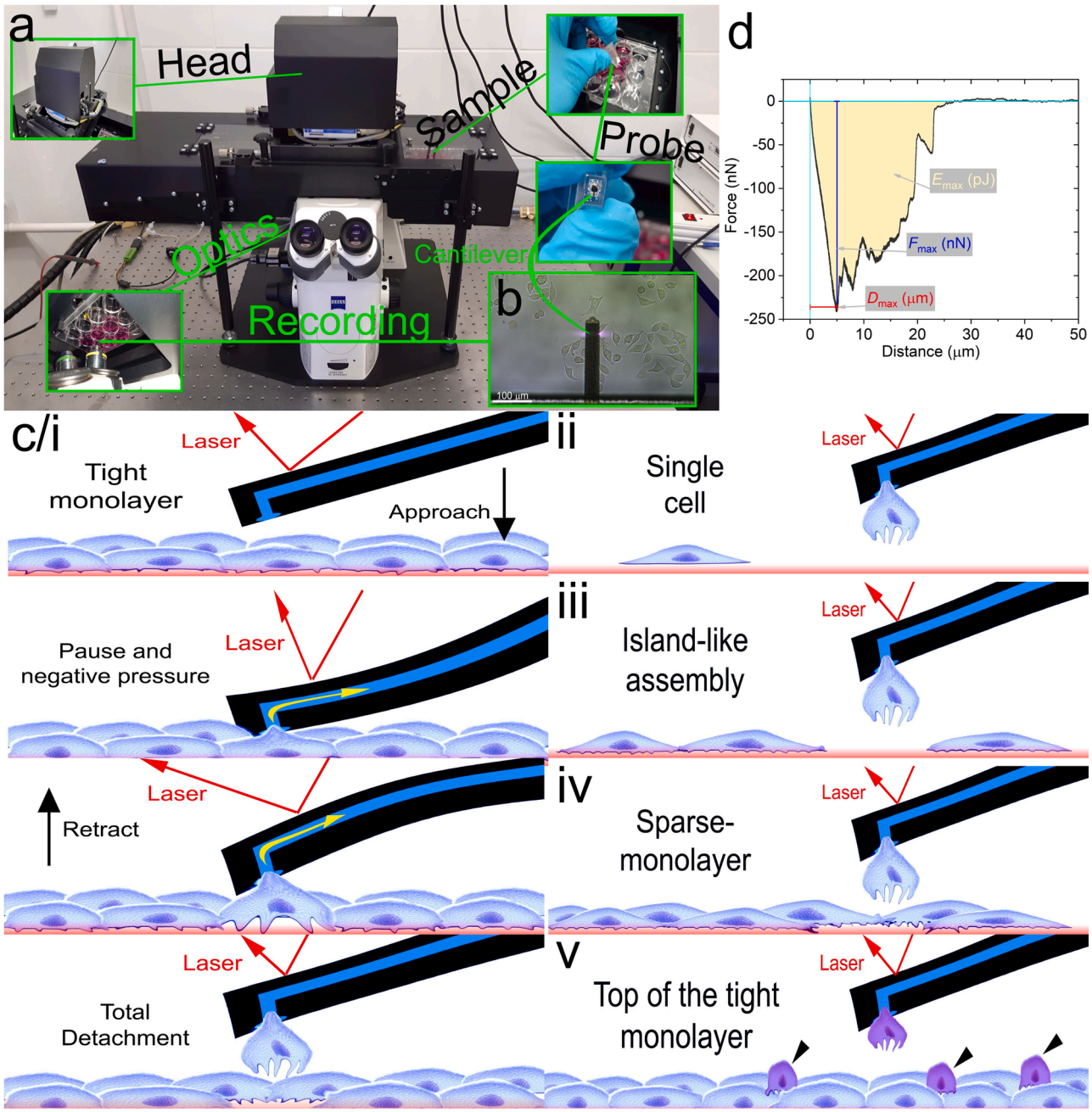

Fig. 1. Schematic representation of the robotic FluidFM measurement setup and procedure. Living cell cultures on the FluidFM (a) can be observed with an optical microscope (see insert b where the cantilever is clearly visible). Under the measurement head, the large area sample stage allows multiple cell targeting in mm-cm scale areas. c) During SCFS recording, the cell from a tight cellular monolayer (i), single cells (ii), cells from island-like assemblies (iii), cells from a sparse monolayer (iv), or cells seeded on top of the tight monolayer (v, black arrowheads) are approached with the hollow FluidFM cantilever, which pauses upon contact with the targeted cell. Subsequently, suction (vacuum) is applied to attach the cell to the aperture, and the cantilever is retracted from the substrate. The retraction results in the total detachment of cells firmly attached, and the SCFS measurement process results in the characteristic FD curves that yield the primary parameters F_{max}, E_{max}, and D_{max} shown in d.

Vero). Cells in different configurations were classified in prior to recording based on 1) their overall distributions and morphology (SC, ISL, ML/CFL, TOP), 2) the size of the cell and its neighbors (tight ML cells are smaller compared to sparse ML cells), 3) the number of neighbors and the number of cells in the group (tight ML 7–8, sparse ML 3–8, ISL 1–6 neighboring cells). The recorded cells were evaluated based on our protocol, FD-curves, and the corresponding SCFS parameters were analyzed with our custom evaluation software (Nagy et al., 2022c). In Fig. 2. the averaged FD-curves of the subcategories show interesting features of cellular adhesion on the various assembly levels. In the Vero cell population, the FD-curves show a strong evolution from the single-cell state to the tight monolayer state (Fig. 2a). In contrast, this type of evolution is absent in HeLa cells, where the FD-curves present similar tendencies (Fig. 2b). It is important to mention that even by looking at averaged FD-curves recorded on individual cells, which may be in various cell-cycle or homeostatic stages, the differences in the SCFS parameters are visible. In Fig. 2c-f. averaged FD-curves of Vero and HeLa cells were compared, which were recorded from similar conditions and confluencies. The single-cell parameters of the investigated categories were evaluated and presented as box charts in Figs. 3 and 4. Statistical

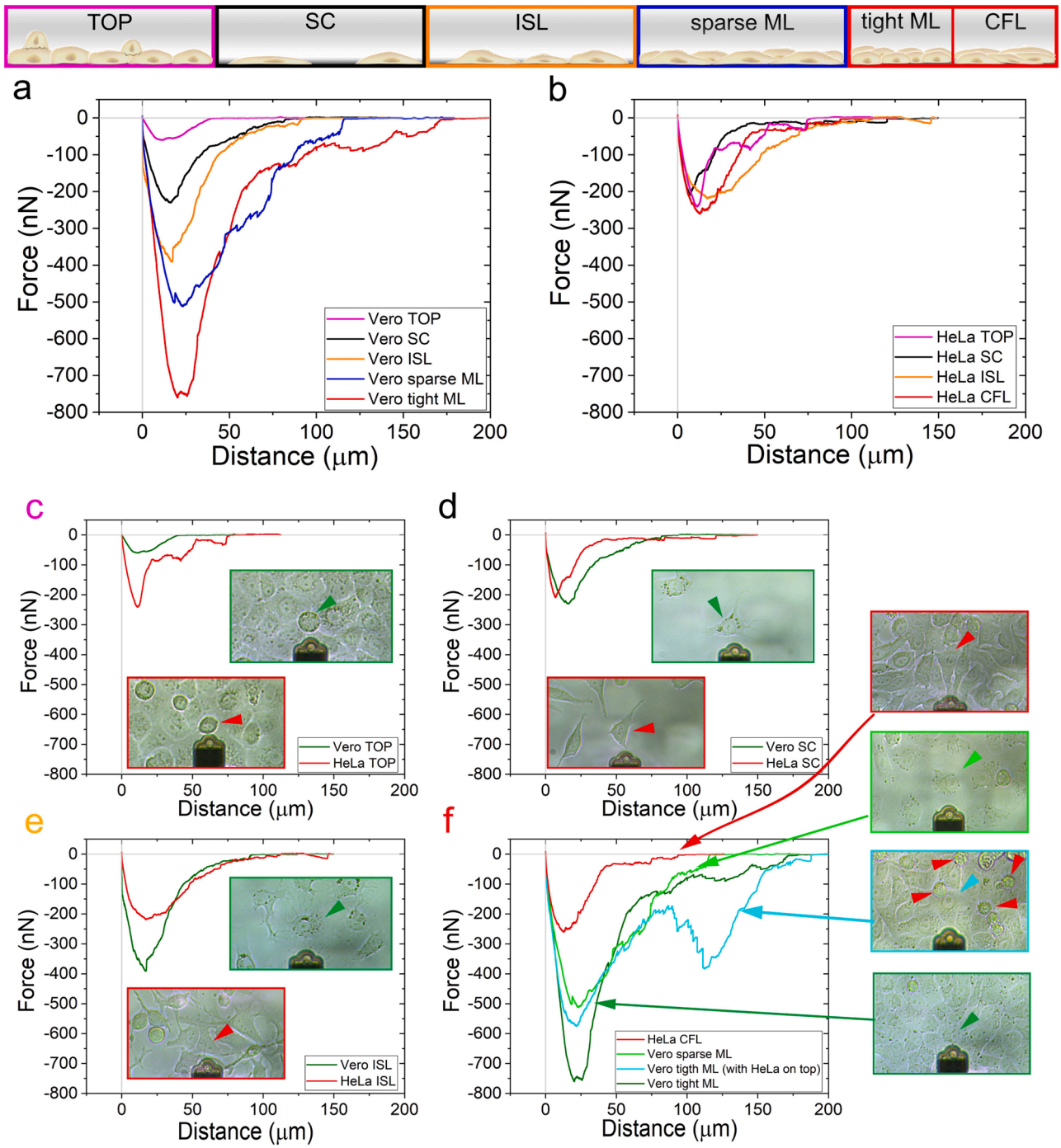

Fig. 2. SCFS results of cells from different categories represented by averaged FD-curves of Vero (a) and HeLa (b) cells. The colors indicate the categories, namely Vero or HeLa cells picked up from the top of the tight Vero monolayer (Vero TOP (a), HeLa TOP (b), magenta), Vero or HeLa single-cells picked up from the gelatin coating (Vero SC (a), HeLa SC (b), black), Vero or HeLa cells picked up from island-like assemblies of same type of cells (Vero ISL (a), HeLa ISL (b), orange), Vero cells picked up from the sparse Vero monolayer (Vero sparse ML (a), blue), and Vero cells pickled up from the tight Vero monolayer or HeLa cells picked up from a confluent HeLa monolayer (Vero tight ML (a), HeLa CFL (b), red). c-d) Comparison of averaged FD-curves of Vero and HeLa cells obtained in the assembly categories and typical microscopic images of the measured cells. c) Vero (green) or HeLa (red) cells were picked-up from the TOP of the Vero tight ML; in the images, olive green arrow points to Vero cell and red arrow to HeLa cell. On d) the single-cell (SC) case, while on e) the island-like (ISL) assembly is shown. f) compares the confluent culture case of HeLa cells with cells detached from Vero monolayers, where three subcategories are presented: the Vero sparse ML case (light green), the Vero tight ML case with HeLa cell influence (turquoise, red arrows point to HeLa cells), and the Vero tight ML case (olive green). (For interpretation of the references to colour in this figure legend, the reader is referred to the web version of this article.)

evaluation was made for the subcategories of comparability. The comparison of cell lines only makes sense in the case of the same morphological category, which means that between Vero and HeLa cells, the evaluation was only made between SC-SC, ISL-ISL, ML-CFL, TOP-TOP cases (Fig. 2). However, the differences in the morphological structure were evaluated for the individual cell lines but not for all subcategories. The Supplementary Information (SI) lists the detailed results of the conducted statistical tests on the different subcategories and also presents the correlations of the various parameters measured (see Figs S1-S2, Tables S1-S3). Also, to elaborate our data further, the exact

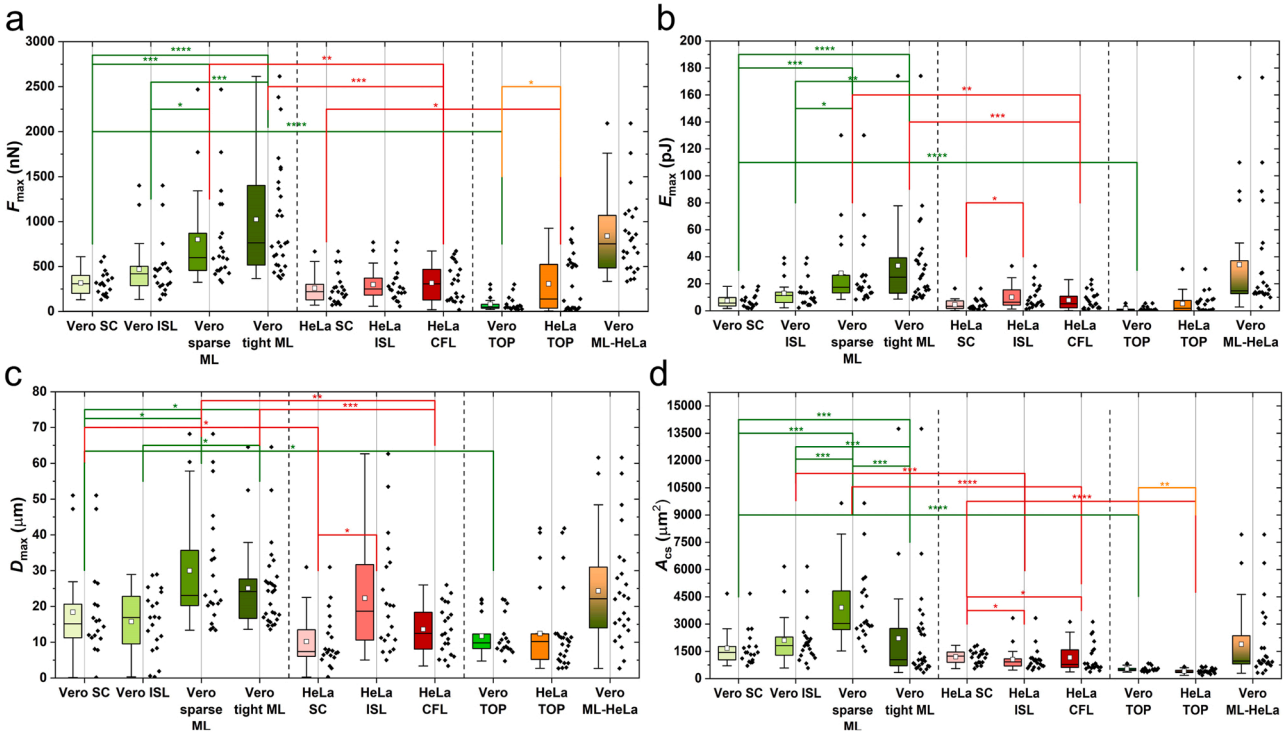

Fig. 3. Population distributions of the measured single-cell adhesion parameters. a) Measured single-cell (SC) F_{max} values in various categories. Values of the categories are: Vero SC 131–609 nN, Vero ISL 134–1401 nN, Vero sparse ML 324–2469 nN, Vero tight ML 367–2615 nN, HeLa SC 71–667 nN, HeLa ISL 57–769 nN, HeLa CFL 19–672 nN, Vero TOP (on tight Vero ML) 23–300 nN, HeLa TOP (on tight Vero ML) 334–1145 nN, Vero ML-HeLa (Vero is picked up from the Vero monolayer while HeLa is influencing the Vero tight monolayer) 334–2093 nN. b) E_{max} parameter of various categories. Values of the categories are: Vero SC 2–18 pJ, Vero ISL 2–39 pJ, Vero sparse ML 8–130 pJ, Vero tight ML 9–174 pJ, HeLa SC 0.2–17 pJ, HeLa ISL 1.3–33 pJ, HeLa CFL 0.1–17 pJ, Vero TOP (on tight Vero ML) 0.2–6 pJ, HeLa TOP (on tight Vero ML) 0.01–31 pJ, Vero ML-HeLa (HeLa is influencing the Vero tight monolayer) 3–173 pJ. c) D_{max} parameter of various categories. Values of the categories are: Vero SC 0.2–51 μm, Vero ISL 0.3–29 μm, Vero sparse ML 13–68 μm, Vero tight ML 14–65 μm, HeLa SC 0.3–31 μm, HeLa ISL 5–63 μm, HeLa CFL 3–26 μm, Vero TOP (on tight Vero ML) 5–22 μm, HeLa TOP (on tight Vero ML) 3–42 μm, Vero ML-HeLa (HeLa is influencing the Vero tight monolayer) 3–62 μm. d) A_{cs} parameter of various categories. Values of the categories are: Vero SC 708–4678 μm^2, Vero ISL 582–6169 μm^2, Vero sparse ML 1521–9649 μm^2, Vero tight ML 339–13741 μm^2, HeLa SC 556–1831 μm^2, HeLa ISL 474–3332 μm^2, HeLa CFL 371–3122 μm^2, Vero TOP (on tight Vero ML) 359–839 μm^2, HeLa TOP (on tight Vero ML) 249–665 μm^2, Vero ML-HeLa (HeLa is influencing the Vero tight monolayer) 302–7922 μm^2.

cell-substrate contact area (A_{cs}) of individual cells was defined based on the recorded microscopic images directly before detachment (see Fig. 3d). This enabled the visualization of area normalized SCFS parameters (Fig. 4b-c) and to calculate cell-cell contact forces based on a model we introduce later in this work (see Fig. 5 and relevant text in the discussions). Furthermore, a newly introduced parameter, the spring coefficient (S_c), the fraction of F_{max} and D_{max}, characterizes the elasticity of a given cell and can be interpreted as its elongation based on its attachment strength and deformation capability (Fig. 4a). The recorded S_c values are analyzed in Fig. 4b.

The significance level was tested with the non-parametric Kolmogorov-Smirnov test because the data was found to have a lognormal distribution, where the value p indicates the level of significant difference between the two categories. The p-value is marked with an asterisk indicating the level of significance, in the case of $p < 0.05$ with *, $p < 0.01$ with **, $p < 0.001$ with ***, and $p < 0.0001$ with ****.

In the analyzed SCFS parameters, F_{max}, E_{max}, and D_{max} are directly exported from the investigated FD-curves, F_{max} is shown in Fig. 3a, where strong significances have been found between the various categories analyzed. The same contact maturation is also observable in the E_{max} parameter shown in Fig. 3b, which shows the same maturation in Vero contacts, while the HeLa cells have different adhesion energies between the SC and ISL states. Shown in Fig. 3c, another characteristic SCFS parameter, the $D_{max,}$ represents the elongation of a cell until the maximum detachment force (F_{max}) is reached. To examine the influence of cell size on SCFS parameters determining cell attachment forces and energies, the exact cell-substrate contact area (A_{cs}) was determined (Fig. 3d). The main differences in A_{cs} are strong between the organization levels of Vero and HeLa cells since the ML/CFL cases in the two cell lines are significantly smaller than SC cases, showing that in an established confluent layer, the cells have reduced area to spread.

The spring coefficient (S_c), representing F_{max}/D_{max} of Vero cells, shows a significantly rising tendency from the SC to the ML state (Fig. 4b). Also, by normalizing the SCFS parameters F_{max} and E_{max} with A_{cs}, significant differences can be observed between Vero tight ML and all other Vero categories (SC/ISL/sparse ML), which can be attributed to the inevitable presence of cell junctions (Fig. 4b-c). Also, Vero tight ML has significantly higher F_{max}/A_{cs} and E_{max}/A_{cs} than HeLa CFL cells, which directly proves loser or less adhered junctions in HeLa cells. A further interesting observation is the attachment force normalized by the cell area when comparing HeLa SC and HeLa TOP cells since the HeLa cells seeded on the Vero monolayer exhibit larger values compared to the HeLa cells picked up from the ECM mimicking gelatin substrate. The coherence and correlation between some measured cell mechanical parameters were depicted on scatter plots (see SI Fig. S1).

In the Vero cell population, the FD-curves show a substantial evolution from the single-cell state to the tight monolayer state, which can be accounted for the development and maturation of cell-cell contacts (Fig. 2a). In Fig. 2c-f. averaged FD-curves of Vero and HeLa cells recorded from similar conditions and confluencies were compared, and here the epithelial assembly and establishment of cell-cell contacts are clearly visible. The range of F_{max} values has a broad spectrum, where Vero cells assembled into a tight and sparse monolayer exhibit the strongest forces onto the substrate. Here, even values up to 2615 nN

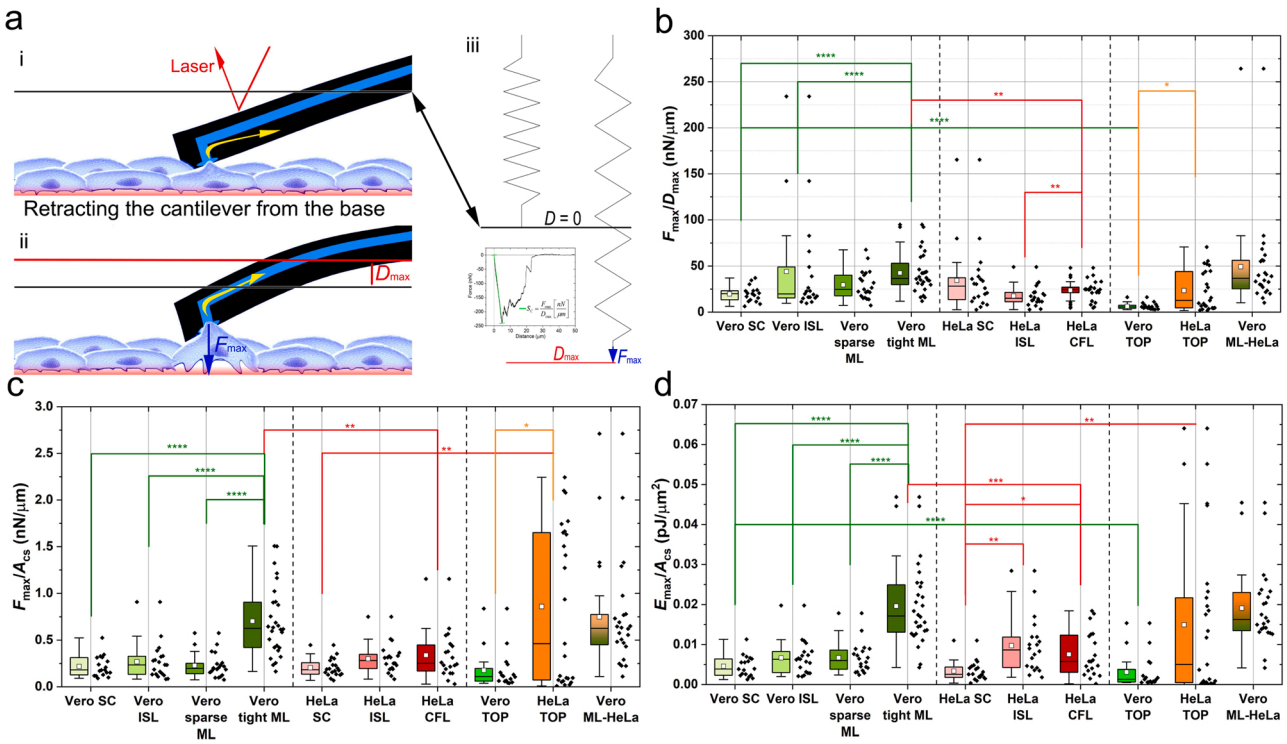

Fig. 4. Spring coefficient (S_c) and the illustration of its physical meaning, and derived single-cell adhesion parameters. a. The elastic capability of the cell shows a deformation upon pulling it from the surface with the FluidFM cantilever (i and ii), which can be interpreted as the pulling of spring with a specific amount of force (iii). The longest elongation D_{max} is reached when pulling the cell with the maximum force F_{max}. Thus the fraction D_{max} and F_{max} yields S_c, the linear slope connecting the maximal force-elongation with the zero level b. S_c parameter of various categories. Values of the categories are: Vero SC 6–37 nN/μm, Vero ISL 10–234 nN/μm, Vero sparse ML 7–68 nN/μm, Vero tight ML 12–95 nN/μm, HeLa SC 3–165 nN/μm, HeLa ISL 3–49 nN/μm, HeLa CFL 5–48 nN/μm, Vero TOP 3–16 nN/μm, HeLa TOP 2–71 nN/μm, Vero ML-HeLa 10–264 nN/μm. c. F_{max}/A_{cs} parameter of various categories. Values of the categories are: Vero SC 0.09–0.52 nN/μm^2, Vero ISL0.08–0.91 nN/μm^2, Vero sparse ML 0.07–0.57 nN/μm^2, Vero tight ML 0.16–1.51 μm^2, HeLa SC 0.07–0.45 nN/μm^2, HeLa ISL 0.08–0.75 nN/μm^2, HeLa CFL 0.03–1.15 μm^2, Vero TOP 0.04–0.84 nN/μm^2, HeLa TOP 0.01–2.24 nN/μm^2, Vero ML-HeLa 0.11–2.71 nN/μm^2. d.) E_{max}/A_{cs} parameter of various categories. Values of the categories are: Vero SC 0.001–0.011 pJ/μm^2, Vero ISL 0.002–0.02 pJ/μm^2, Vero sparse ML 0.002–0.018 pJ/μm^2, Vero tight ML 0.004–0.047 pJ/μm^2, HeLa SC 3.6X(10^{-4})– 0.01 pJ/μm^2, HeLa ISL 0.001–0.03 pJ/μm^2, HeLa CFL 1.77 × $10^{(-4)}$-0.02 pJ/μm^2, Vero TOP 5.2 × $10^{(-4)}$–0.015 pJ/μm^2, HeLa TOP 1.5 × $10^{(-5)}$–0.064 pJ/μm^2, Vero ML-HeLa 0.004–0.045 pJ/μm^2.

have been measured, while in other cases, these values were much lower: F_{max} values of Vero SC are significantly lower to the Vero ML cases ($p < 0.0001$), but not to the ISL assembly, and there is no significant difference between the Vero SC and HeLa SC/ISL/CFL categories either. This means that Vero SC and all of the HeLa categories attach with the same amount of focal force to the substrate. In contrast, HeLa does not show any development in force maturation, which indicates non-existent cell-cell junctions, while in Vero ML assembly, the cell-cell adhesions play a tremendous role. Furthermore, Vero cells detached from ML with HeLa influence were found to be non-different in any of the investigated parameters compared to healthy sparse/tight Vero ML (Figs. 3. and 4.). The stiffer a cell, the shorter the D_{max} distance, and more elastic cells have larger D_{max}. It is known that cancer cells decrease endothelial cell stiffness (Mierke, 2011), but HeLa cells did not alter the epithelial Vero monolayer in this setting (Fig. 3**c**). However, importantly again, the contact maturation of Vero monolayer can be emphasized for D_{max} in contrast to HeLa cells. Vero cells organized into a sparse or tight monolayer become more elastic than SC or ISL assemblies, but HeLa cells organized into ISL structures exhibit larger D_{max} values, and it can be said that generally, HeLa cells are stiffer compared to Vero cells. The higher D_{max} values of HeLa ISL compared to the HeLa SC category indicate increased flexibility of cancer cells organized into multicellular structures (Clark and Vignjevic, 2015), which may signify increased malignancy (Xu et al., 2012).

A feature of Vero cells is that during the formation of monolayers, they go through a stage when cells are widely spread compared to other levels of organization. It is essential since the Vero sparse ML cells exhibit similar SCFS characteristics to tight ML cells, but their A_{cs} are more extensive than all other categories. The F_{max} and E_{max} parameters show differences in the Vero and HeLa cells picked up from the TOP of the Vero monolayer. Also, an observation can be made when comparing Vero and HeLa TOP cells cell-surface area, where HeLa TOP A_{cs} is significantly smaller; however, when comparing Vero and HeLa SC cells, there is no statistical difference. The spring coefficient (S_c), representing F_{max}/D_{max}, of Vero cells shows a significantly rising tendency from the SC to the ML state, which means that in the confluent and tight monolayers, cells present higher elasticity (Fig. 4b) compared to single-cell state and island-like assemblies. However, it should be considered that this elevation in S_c is also caused by the pulling of the cells as a layer with a strong contact to other cells. Significantly higher S_c values were also observed between HeLa cells, but based on the previous results, the HeLa do not form strong cell-cell contacts, and this increased elasticity may be a sign that some kind of support mechanism is formed. Furthermore, the S_c shows also a significant difference between HeLa and Vero cells picked up from the TOP of the ML, which is somewhat expected since cancer cells require higher elasticity when infiltrating a cell layer. Also, another interesting significant difference is between Vero SC and Vero TOP, where the TOP cells show reduced SCFS parameters compared to SC's, which can be explained by the different bidirectional mechanical properties of cells and different substrates (Mierke, 2021) (gelatin in case of SC, and cellular monolayer in case of TOP).

A previous study with FluidFM on HUAEC cells revealed that EMT influences cell-cell and cell-matrix mechanobiological features, and also

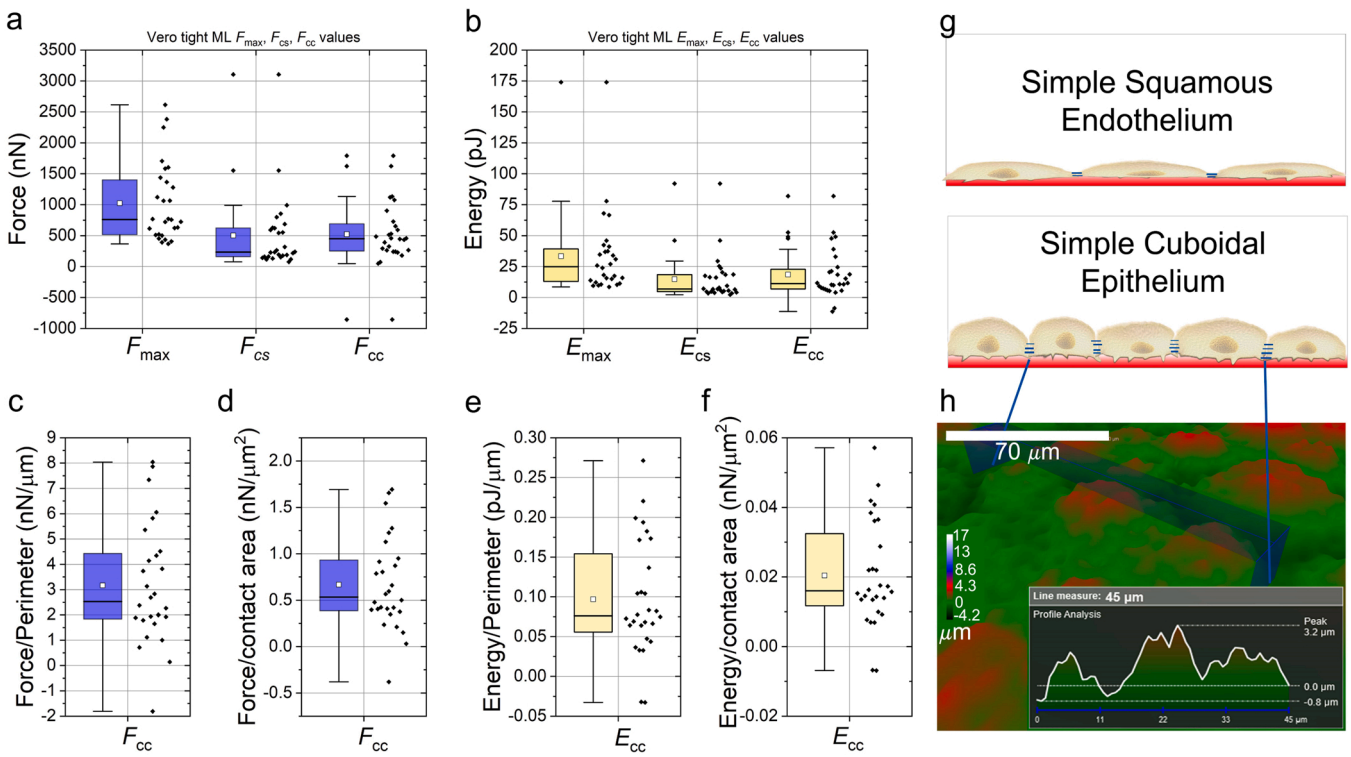

Fig. 5. Distributions of total, cell-substratum, and cell-cell forces and energies of Vero cell from tight monolayers. Based on the proposed formalism, cell-substrate forces (a, F_{cs}) and energies (b, E_{cs}) are a fraction of the total cell detachment forces (a, F_{max}) and energies (b, E_{max}) of cells from the monolayer and have a similar average compared to cell-cell (F_{cs}, E_{cs}) values. By determining the perimeter and the average cell-cell contact, height force and energy (work of adhesion) densities con be calculated (c-f). On g, the morphological differences of the endothelium and kidney epithelial cells are presented, which yield a difference in cell-cell adhesion properties due to the differences in cell-cell contact height. The cell-cell contact height for the kidney epithelium (Vero) was determined using phase holographic images (h).

the cell-cell contact maturation of the endothelial cells was tested (Sancho et al., 2017). Sancho et al. assumed that the averaged cell-cell contact strength can be calculated by directly subtracting averaged individual single-cell forces from averaged detachment forces of monolayer origin. This assumption in our case resulted in 1024 nN average ML force and 316 nN average SC force in Vero cells, which subtracted from each other equals to 707 nN averaged cell-cell adhesion forces in tight ML conformation, which value is approximately twice of the value measured by Sancho et al. This finding is understandable when looking at the morphology of the compact Vero and HUAEC layers since Vero cells are cuboidal and endothelial cells are squamous in morphology, so Vero cells have higher cell-cell borders (Silverthorn, 2016). However, the mentioned procedure with averaging has a substantial limitation since that data of individual cells are lost in the averaging, and the distributions of various parameters cannot be investigated. Also, other aspects must be considered when addressing cell-cell adhesion forces: i) single-cells can undergo different cell cycle events, influencing cell adhesion and traction (Nagy et al., 2022a; Vianay et al., 2018; Panagiotakopoulou et al., 2018; Jones et al., 2019, 2018; Salánki et al., 2021; Gupta et al., 2021); ii) area of single-cells and monolayer origin are significantly different, which heavily influence the number of focal connections and the distance between individual cell-matrix contacts; iii) subtracting a distinct subpopulations average from another subpopulations average may lose single-cell data; iv) cell-cell contacts are not present in single-cells, which influences the arrangement of actin filaments and so a cell's mechanistic features (Vasquez et al., 2017; Mao and Baum, 2015).

Here, we introduce a novel strategy to address the critical question of cell-cell adhesion strength based on experimental data. Our methodology also considers the area and perimeter of various individual cells organized into a tight monolayer. Based on the results, the area-normalized detachment force (F_{max}/A_{cs}) and work (E_{max}/A_{cs}) are an ideal starting point to calculate cell-cell contact forces and energies, where both of these values are significantly higher ($p < 0.0001$) in monolayer detachments than of single-cells as expected, but they are also significantly higher compared to island-like assemblies and sparse monolayers. The cell-substrate contact area normalized values represent the work (e_{cs}) and force (f_{cs}) surface density of a given cell. According to our model, F_{max} can be split up to two parts, namely the cell-substrate and the cell-cell interaction contributions (Eq. 1).

$$F_{max} = f_{cs} * A_{cs} + F_{cc} \tag{1}$$

Where A_{cs} is the contact area of the cell and the substratum of a given cell picked up from a tight monolayer, and F_{cc} is the force between the cell and the cells directly surrounding it. We also propose a similar equation for the adhesion energy (Eq. 2).

$$E_{max} = e_{cs} * A_{cs} + E_{cc} \tag{2}$$

Here, E_{cc} is the adhesion energy (work of adhesion) contribution of the cell-cell contacts of the investigated cell.

Next, we assume that the averaged cell-substratum force and work densities are alike in the SC, ISL, and sparse ML state, so f_{cs} and e_{cs} can also be considered the same when the Vero cells are in the sparse and tight monolayer configuration. Based on this assumption and using the individual cell areas measured by microscopy from the tight Vero ML, and Eqs. 1 and 2, we separated the adhesion force and work in the case of the tight monolayer into the two fundamental components. The results are plotted in Fig. 5. It should be emphasized that considering the individual cell areas and employing the above assumption, an average cell-cell adhesion force of 523 nN and average cell-cell adhesion work of 18.5 pJ were obtained.

It is also interesting to investigate the origin of the cell-cell adhesion

force and work. Our values are much larger than those obtained by Sancho et al. (2017). We believe that the explanation of this difference is the larger cell-cell contact surface area between the Vero cells compared to the HUAEC cells (see Fig. 5g). To consider this, we determined the perimeter of the individual cells and calculated force and work contribution of a unit contact length based on these respective cell perimeters (P_c). Based on Eq. 3 (and a similar equation for the work), by using an averaged cell contact height (h_{cc}) of 4.75 micrometers from phase holographic imaging experiments (see Fig. 5h), we could calculate the averaged cell-cell contact force (F_{cc}) (and work (E_{cc})) for a unit cell-cell contact area (A_{cc}), where $A_{cc}=h_{cc}*l_c$. The obtained results are 0.67 ± 0.5 nN/μm^2 (6.7 ×10$^{(-4)}$ N/m^2) cell-cell contact force density and 0.02 ± 0.015 pJ/μm^2 (2 ×10$^{(-8)}$ J/m^2) cell-cell contact work density on average, which values are ~3 times higher than in the experienced cell-substratum force and work densities of Vero SC, ISL, and sparse ML conformations.

$$F_{cc} = f_{cc} * h_{cc} * l_c \tag{3}$$

3. Conclusions

Summarized, we measured the adhesion maturation of SCFS parameters in kidney epithelial Vero cells and cancerous HeLa cells with particular regard to individual cell area and perimeter, which allowed to determine the exact force and energy (work of adhesion) densities of single-cell contacts. By observing that the force and work densities of Vero cells detached from tight monolayers were significantly higher compared to cells organized into single, island-like, and sparse monolayer assemblies, we introduced an equation, which incorporates individual cell areas of the tight monolayer, to determine the forces and energies of cell-substratum and cell-cell contacts. Respective perimeters and average cell-cell contact height from holographic images have revealed the cell-cell contact areas with cells surrounding the investigated monolayer cells, which allowed us to determine the cell-cell contact force and energy densities. The results show that cell-cell contact strength plays a major role in the case of simple cuboidal epithelium and is higher than cells of other configurations only presenting focal adhesions. A reason for this increase is that within monolayers, stresses are propagated over several cell diameters by intercellular adhesion, and monolayer elasticity is two orders of magnitude larger than the elasticity of their isolated cellular components (Hannezo et al., 2014; Harris et al., 2012). Therefore, monolayers could withstand more than a doubling in length before failing through the rupture of intercellular junctions. Since mechanosensitivity and the release of serotonin is known in the gastrointestinal-tract epithelium (enterochromaffin cells) (Beyder, 2019), and the kidney epithelium (Vero cells) must also withstand external forces and stresses, the question arises how kidney function depends on intercellular connectivity, for which investigations our study also present a relevant methodology. Furthermore, based on the observations the squamous endothelium has different adhesion intercellular adhesion strength compared to the cuboidal epithelium, which raises the question whether the phenotype of cell lines plays a major role in interconnectivity resulting in different functionalities and substance transport mechanism. For a strong intercellular connection the blood-brain-barrier (BBB) is a well-known organization of endothelial cells, which provides a tightly sealed layer to prevent entry of substances and damaging agents (Kadry et al., 2020; Dietrich, 2002). Also, pseudostratified epithelia, commonly found in the respiratory airways, has a punakoid morphology (Iber and Vetter, 2022), which enables various forms and strength in intercellular connectivity. Therefore, not only the cellular morphology but the origin and organ specificity of the cells is an important aspect of cell-cell contact strength. From another perspective extracellular ion concentrations heavily influence intercellular and basal contact strength by altering receptor affinity (Tobey et al., 2004; Shen et al., 2021; Leitinger et al., 2000; Brown et al., 2018). Among other physiologically relevant ions and molecules an important ion is the calcium (Ca^{2+}), which has a versatile and fundamental role in protein function, cell signaling, transcription, homeostasis, mitochondrial function, metabolism and cancer development (Milles et al., 2018; Shen et al., 2021; Logan et al., 2022; Bagur and György, 2018; Dejos et al., 2020). Therefore, the investigation of ion versatility and its effect on cell monolayer development and integrity (especially in endothelial layers since the blood has a relatively large ion concentration variation) is of high interest, and their role in cell-cell and cell-substratum adhesions could be investigated as a possible continuation of our work.

Another exciting aspect of our study is that HeLa cancer cells have limited variations in the observed SCFS parameters. However, some differences are present between single-cell and confluent state, which gives the impression of the absence of strong cell-cell contacts, proving that cancer cells are unique in this aspect and that their adhesion and survival is independent of colony formation. Furthermore, cancerous HeLa cells seeded on top of the Vero monolayer exhibit significantly larger adherence compared to non-cancerous Vero cells also seeded on top of the monolayer. Therefore, we conclude that cancer cells present adhesion proteins essential for strong intercellular attachments to infiltrate monolayers. From the literature, the proteins needed for intercellular adhesion between cancer cells or white blood cells attach to the endothelium or exit the bloodstream via VCAM, PECAM, ICAM, EPCR, TM-integrin interactions (Park and Shimaoka, 2020; Gordon et al., 2020). Based on our observation, the membrane proteins present on the apical surface of Vero cells may promote excessively high adherence of cancerous HeLa cells (Nagy et al., 2022b; Harjunpää et al., 2019; Guo et al., 2014). So, the reason Vero cells do not adhere to the monolayer as strong as HeLa cells is the special expression composition of adhesion receptors by HeLa cells, which seem to have a ligand on the apical Vero monolayer surface. The nature of this ligand-receptor interaction could elucidate the mechanisms of cancer cell invasion of tissues, and its potential disruption may decrease the probability of metastasis formation.

However, novel protocols on FluidFM must be considered to study transendothelial migration of cancer cells since it was presented that flow and shear-stress influences cancer cell adhesion to monolayers, their transmigration capabilities, endothelial stiffness, and protein expression patterns (Gordon et al., 2020; Brandsma et al., 2002). We propose developing a custom-made, standard-size plate with half-pipes etched through that enable fluidic flow, circulated by a pump, and accessed by the FluidFM probe. The half-pipes can then be covered with ECM mimicking gels, and endothelial cells could be seeded there to create a barrier between the ECM and the fluid. Cancer cells added to the circulating fluid can then freely move in the endothelial half-pipes, and their adhesion strength could be studied under 3D in vitro conditions. Also, FluidFM would enable the extraction of intracellular content of the infiltrated endothelium, and with common techniques used in molecular biology and genetics (e.g., qPCR) the mRNA contents and altered protein expression of infected layers can be studied (Chen et al., 2022), with special regard to the exact migration spot. This method would also show the importance and strength of apical adhesion proteins in cancer-related infiltration processes. Furthermore, cell-cell adhesion in fertilization can also be accessed with the presented multilayer methodology upon growing simple columnar epithelium from the uterus and then investigating environmental effects on blastocyst adherence and implantation.

4. Materials and methods

4.1. Gelatin coating

For the coating, 0.02 % gelatin in Dulbecco's phosphate buffered saline (DPBS) solution was freshly prepared. The 6-well non-coated culture plates used in the experiments were filled in each well with 1 mL gelatin solution and placed into the incubator for 20 min at 37 °C. The coated dish was then rinsed 3x with PBS and filled with 3 mL of

completed culture media until utilization. The ultra-thin gelatin layer applied was already characterized previously by our group with QCM, OWLS, EPIC BT biosensor, and atomic force-microscope (AFM), and its thickness was measured to be around 10 nm (Debreczeni et al., 2020).

4.2. Cell culture techniques

Vero (ATCC CCL81) and HeLa (ECACC 93021013) cultures were maintained inside a humidified incubator at 37 °C and 5 % CO_2. For culturing, completed culture medium consisting of Dulbecco's modification of Eagle Medium (DMEM, Gibco) extended with 10% heat-inactivated fetal bovine serum (FBS, Biowest), 4 mM L-glutamine, 100 U/mL penicillin, and 100 μg/mL streptomycin solution. For Vero cells, 2 mM L-glutamine, sodium pyruvate, and MEM non-essential amino acid solution were specially added into the DMEM (Ammerman et al., 2008). Reagents were obtained from Sigma-Aldrich.

To create different cell culture confluency levels for the experiments, Vero or HeLa cells were picked up from confluent cell cultures using 0.05 % (w/v) trypsin- and 0.02 % (w/v) EDTA-DPBS solution for 2 min to detach cells from the tissue culture dish. Then, detached cells in different concentrations (0.6×10^6–0.24×10^6–0.12×10^6 cells) were added to the wells of the previously gelatin-coated 6-well dish. The 6-well plate was then placed into a humidified incubator for 24 h at 37 °C and 5 % CO_2 to let cells adhere and spread on the gelatin coating. After the elapsed time, wells were rinsed with DPBS and were filled with HPMI buffer (9 mM glucose,10 mM $NaHCO_3$, 119 mM NaCl, 9 mM HEPES, 5 mM KCl, 0.85 mM $MgCl_2$, 0.053 mM $CaCl_2$, 5 mM Na_2HPO_4 $\times 2\ H_2O$, pH 7.4) for the recording.

To record Vero and HeLa cell adherence to Vero monolayers, cells were detached from the culture dishes as described above, cell suspensions were centrifuged for 5 min at 200xg, the cell pellets were resuspended in 1 mL HPMI buffer and 0.24×10^6 cells were distributed on top of the established Vero tight monolayer. Before adding Vero and HeLa cells to the Vero monolayer containing plate, the monolayer was rinsed, floating cells (apoptotic, dead) were washed out with DPBS, and HPMI buffer was added as an experimental medium. Newly added to the top of the Vero monolayer Vero and HeLa cells were allowed to adhere for 30 min before starting the recording.

4.3. High-throughput SCFS recordings with robotized FluidFM

For the SCFS recordings, the FluidFM OMNIUM instrument (Cytosurge AG., Zürich, Switzerland) placed on a vibration-free table was used. Cells cultured in the 6-well plate containing were placed into the robotized xy-stage of the instrument, observed with Zeiss Axio Observer Z1 optical microscope (Carl Zeiss AG, Oberkochen, Germany). Buffer filled FluidFM micropipette cantilevers were mounted on the z-stage of the instrument, known as head. The stage of the OMNIUM can handle two separate plates, from which one is the experimental plate and the other one is utilized for cleaning purposes or probe exchange. After each recording conducted on living cells the cantilever attached to the plastic holder known together as probe, is dipped in MQ water followed by a few seconds of 5 % hypochlorite, then rinsed again 4 times with MQ water. Before each SCFS recording cycle the inverse optical lever sensitivity (*InvOLS*) is determined because its accuracy influences the obtained force values, which is dependent on the actual laser-spot position from the laser reflection optics of the instrument (Nagy et al., 2019). The spring constant (k) of the cantilever is calculated in air before dipping the cantilever into buffer, by the built-in function of the OMNIUM using the Sader-method as calibration strategy (Sader et al., 2012). *InvOLS* must be defined for the laser-spot positions used during recordings and k for every individual cantilever to receive the most accurate results with the smallest error as possible (Nagy et al., 2019). For SCFS recording an 8 μm aperture FluidFM micropipette cantilever was used, and recording execution was done with parameters of recording as following: set-point 20 mV, approach and retract speed 1 μm/s, pressure − 500 mbar, pause 5 s, retraction distance 150 μm. Before each recording, a microscopy image was taken of the cell to be detached to evaluate cell area and to validate their category. In total 13 experimental sessions were conducted including the various scenarios described in the manuscript. During these recordings a total of 5 cantilevers were used with spring constant values in the range of 1.5–2.3 N/m.

4.4. Data evaluation

Analysis of the obtained SCFS data was carried out using a custom Matlab application written by us to evaluate the characteristic FD-curves and save all numeric parameters automatically for quicker evaluation (Nagy et al., 2022c). Cell-substrate contact area (A_{cs}) and cell perimeter (P_c) were determined in CellProfiler (Carpenter et al., 2006), which is capable of switching between images and saving the results automatically after the user is able to draw the outline shape of the cell manually. The area and perimeter of a cell is calculated in pixels, where 1 px = 5.0625 μm^2 and the length of a pixel is 2.25 μm. Data plots and significance tests were performed in Origin 9.5. By testing the normality and log-normality of the data it became clear, that the categories count indeed as absolutely separated, and they cannot be confused with one another. This can be stated, because the data for all HeLa and Vero cells respectively did not pass the normality and log-normality tests, but the established categories did. Therefore, general diagrams and statistical comparisons can only be made between the categorically separated HeLa and Vero data. Since the obtained data is rather log-normally distributed for all parameters, but the subpopulation sample sizes indicate to use a statistical test designed for log-normally distributed data, for the final evaluation the Kolmogorov-Smirnov test (two-sample, unpaired) was applied. Results of normality and log-normality tests, histograms of log-normal fitting on subpopulations, FD-curves of individual cell belonging to subpopulations, and other relevant data is shown in the Supplementary information (SI Tables S1-S3).

4.5. Digital holographic microscopy

The digital holographic cytometer, Holomonitor M4 (Phase Holographic Imaging PHI AB, Lund, Sweden) was placed inside a humidified incubator with 37 °C and 5% CO_2. Vero cell spreading and growth was monitored for 24 h, during which they established a confluent monolayer on a gelatin-coated 35 mm glass bottom dish (VWR). Gelatin coating was performed as described above, and for the recording the dish was filled with 3 mL of completed cell culture medium. Prior to the recording 200 μl cell suspension (~6×10^5 cells) were added to the 35 mm gelatin-coated dish, which was covered with the HoloLid (Phase Holographic Imaging PHI AB, Lund, Sweden). The set-up of the Holomonitor and the HoloLid are determined by the manufacturer, and all guidelines were followed according to the manual.

CRediT authorship contribution statement

Ágoston G. Nagy, PhD Student: Experimental design and execution, data acquisition and evaluation, graphic design, wrote the paper. Inna Székács, PhD, Senior Research Fellow: Cell culture and maintenance, work coordination, experimental design and execution, data acquisition, paper revision. Attila Bonyár, PhD, Associate Professor: data interpretation, work coordination, revised the paper. Robert Horvath, PhD, Head of Laboratory: working hypothesis, experimental design, data interpretation, work coordination, revised and coordinated the paper.

Competing Interests

The authors declare no competing interests.

Data Availability

All data generated or analyzed during this study are included in this published article and its supplementary information files.

Acknowledgments

Szilvia Bősze kindly provided Vero kidney epithelial cells and HPMI buffer from the Research Group of Peptide Chemistry, Department of Organic Chemistry, Eötvös L. University, Budapest, Hungary. This work was supported by the "Lendület" (HAS) research program, the National Research, Development and Innovation Office of Hungary (VEKOP, ELKH topic-fund, "Élvonal" KKP_19 KKP 129936 and KH grants, TKP2022-EGA-04 program financed from the NRDI Fund). The research reported in this paper and partially carried out at the Budapest University of Technology and Economics has been supported by the National Research Development and Innovation Fund (TKP2020) based on the charter of bolster issued by the National Research Development and Innovation Office under the auspices of the Ministry for Innovation and Technology. This research was also funded by the National Research, Development, and Innovation Fund of Hungary under Grant TKP2021-EGA-02.

Appendix A. Supporting information

Supplementary data associated with this article can be found in the online version at doi:10.1016/j.ejcb.2022.151273.

References

Ammerman, N.C., Beier-sexton, M., Azad, A.F., 2008. Growth and maintenance of vero cell lines. Curr. Protoc. Microbiol. 1–7. https://doi.org/10.1002/9780471729259.mca04es11.
Aramesh, M., et al., 2019. Localized detection of ions and biomolecules with a force-controlled scanning nanopore microscope. Nat. Nanotechnol. 14.
Bagur, R., György, H., 2018. Intracellular Ca2+ sensing: role in calcium homeostasis and signaling. Mol. Cell 66, 780–788.
Benoit, M., Gabriel, D., Gerisch, G., Gaub, H.E., 2000. Discrete interactions in cell adhesion measured by single-molecule force spectroscopy. Nat. Cell Biol. 2, 313–317.
Beyder, A., 2019. In pursuit of the epithelial mechanosensitivity mechanisms. Front. Endocrinol. 9, 1–5.
Bhat, A.A., et al., 2019. Tight junction proteins and signaling pathways in cancer and inflammation: a functional crosstalk. Front. Physiol. 10, 1–19.
Brandsma, D., et al., 2002. Vascular cell adhesion molecule-1 is a key adhesion molecule in melanoma cell adhesion to the leptomeninges. Lab. Investig. 82, 1493–1502.
Brown, K.L., Banerjee, S., Feigley, A., Abe, H., Timothy, S., 2018. Salt-bridge modulates differential calcium-mediated ligand binding to integrin α 1- and α 2-I domains. Sci. Rep. 1–14. https://doi.org/10.1038/s41598-018-21231-1.
Carpenter, A.E., et al., 2006. CellProfiler: image analysis software for identifying and quantifying cell phenotypes. Genome Biol. 7.
Chen, W., et al., 2022. Live-seq enables temporal transcriptomic recording of single cells. Nature 608, 733–739.
Claesson-welsh, L., Dejana, E., Mcdonald, D.M., 2021. Permeability of the endothelial barrier: identifying and reconciling controversies. Trends Mol. Med. 27, 314–331.
Clark, A.G., Vignjevic, D.M., 2015. Modes of cancer cell invasion and the role of the microenvironment. Curr. Opin. Cell Biol. 36, 13–22.
Davidenko, N., et al., 2016. Evaluation of cell binding to collagen and gelatin: a study of the effect of 2D and 3D architecture and surface chemistry. J. Mater. Sci. Mater. Med. 27.
Debreczeni, M.L., et al., 2020. Human primary endothelial label-free biochip assay reveals unpredicted functions of plasma serine proteases. Sci. Rep. 10, 1–14.
Dejos, C., Gkika, D., Cantelmo, A.R., 2020. The two-way relationship between calcium and metabolism in cancer. Front. Cell Dev. Biol. 8, 1–14.
Dietrich, J., 2002. The adhesion molecule ICAM-1 and its regulation in relation with the blood – brain barrier. J. Neuroimmunol. 128, 58–68.
Friedl, P., Wolf, K., 2003. Tumor-cell invasion and migration: diversity and escape mechanisms. Nat. Rev. Cancer 3, 362–374.
Friedl, P., Locker, J., Sahai, E., Segall, J.E., 2012. Classifying collective cancer cell invasion. Nat. Cell Biol. 14, 777–783.
Friedrichs, J., et al., 2013. A practical guide to quantify cell adhesion using single-cell force spectroscopy. Methods 60, 169–178.
Gäbelein, C.G., Feng, Q., Sarajlic, E., Zambelli, T., Guillaume-gentil, O., 2021. Mitochondria transplantation between living cells. bioRxiv 1–30. https://doi.org/10.1101/2021.11.09.467932.
Gerecsei, T., et al., 2019. Journal of colloid and interface science adhesion force measurements on functionalized microbeads: an in-depth comparison of computer controlled micropipette and fluidic force microscopy. J. Colloid Interface Sci. 555, 245–253.
Gerecsei, T., et al., 2021. Dissociation constant of integrin-RGD binding in live cells from automated micropipette and label-free optical data. Biosensors 11, 1–11.
Gordon, E., Schimmel, L., Frye, M., Gordon, E., 2020. The importance of mechanical forces for in vitro endothelial cell biology. Front. Physiol. 11, 1–20.
Guillaume-Gentil, O., et al., 2014. Force-controlled manipulation of single cells: from AFM to FluidFM. Trends Biotechnol. 32, 381–388.
Guillaume-Gentil, O., et al., 2016. Tunable single-cell extraction for molecular analyses. Cell 166, 506–517.
Guillaume-Gentil, O., et al., 2017. Single-cell mass spectrometry of metabolites extracted from live cells by fluidic force microscopy. Anal. Chem. 89, 5017–5023.
Guo, D., Zhu, Q., Zhang, H., Sun, D., 2014. Proteomic analysis of membrane proteins of vero cells: exploration of potential proteins responsible for virus entry. DNA Cell Biol. 33, 20–28.
Gupta, V.K., Nam, S., Camuglia, J., Martin, J.L., 2021. The nature of cell division forces in epithelial monolayers. J. Cell Biol. 220.
Haber, A.L., et al., 2017. A single-cell survey of the small intestinal epithelium. Nature 551, 333–339.
Hannezo, E., Prost, J., Joanny, J., 2014. Theory of epithelial sheet morphology in three dimensions. PNAS 111, 27–32.
Harjunpää, H., Asens, M.L., Guenther, C., Fagerholm, S.C., 2019. Cell adhesion molecules and their roles and regulation in the immune and tumor microenvironment. Front. Immunol. 10.
Harris, A.R., et al., 2012. Characterizing the mechanics of cultured cell monolayers. PNAS 109, 16449–16454.
Heintzman, N.D., et al., 2009. Histone modifications at human enhancers reflect global cell-type-specific gene expression. Nature 459, 3–7.
Helenius, J., Heisenberg, C.-P., Gaub, H.E., Muller, D.J., 2008. Single-cell force spectroscopy. J. Cell Sci. 121, 1785–1791.
Helfricht, N., Mark, A., Dorwling-Carter, L., Zambelli, T., Papastavrou, G., 2017. Extending the limits of direct force measurements: colloidal probes from sub-micron particles. Nanoscale 9, 9491–9501.
Hirt, L., Gr, R., Berthelot, T., Cornut, R., 2015. Local surface modification via confined electrochemical deposition with FluidFM. RSC Adv. 5, 84517–84522.
Hirt, L., Reiser, A., Spolenak, R., Zambelli, T., 2017. Additive manufacturing of metal structures at the micrometer scale. Adv. Mater. 201604211, 1–30.
Iber, D., Vetter, R., 2022. 3D organisation of cells in pseudostratified epithelia. Front. Phys 1–8.
Jaczewska, J., et al., 2014. TNF-α and IFN-γ promote lymphocyte adhesion to endothelial junctional regions facilitating transendothelial migration. J. Leukoc. Biol. 95, 265–274.
Jones, M.C., Askari, J.A., Humphries, J.D., Humphries, M.J., 2018. Cell adhesion is regulated by CDK1 during the cell cycle. J. Cell Biol. 217, 3203–3218.
Jones, M.C., Zha, J., Humphries, M.J., 2019. Connections between the cell cycle, cell adhesion and the cytoskeleton. Philos. Trans. R. Soc. B Biol. Sci. 374, 1–10.
Kadry, H., Noorani, B., Cucullo, L., 2020. A blood – brain barrier overview on structure, function, impairment, and biomarkers of integrity. Fluids Barriers CNS 17, 1–24.
Kanyo, N., et al., 2020. Glycocalyx regulates the strength and kinetics of cancer cell adhesion revealed by biophysical models based on high resolution label-free optical data. Sci. Rep. 10, 1–20.
Kiesslich, S., Kamen, A.A., 2020. Vero cell upstream bioprocess development for the production of viral vectors and vaccines. Biotechnol. Adv. 44.
Knust, E., 2002. Regulation of epithelial cell shape and polarity by cell-cell adhesion (review). Mol. Membr. Biol. 19, 113–120.
Koehler, M., et al., 2021. Reovirus directly engages integrin to recruit clathrin for entry into host cells. Nat. Commun. 12, 1–15.
Kozyrina, A.N., Piskova, T., Russo, J.Di, 2020. Mechanobiology of epithelia from the perspective of extracellular matrix heterogeneity. Front. Bioeng. Biotechnol. 8.
Leitinger, B., Mcdowall, A., Stanley, P., Hogg, N., 2000. The regulation of integrin function by Ca 2 ‡. Biochim. Biophys. Acta 1498, 91–98.
Li, M., Liu, L., Zambelli, T., 2022. FluidFM for single-cell biophysics. Nano Res. 15, 773–786.
Lock, J.G., et al., 2018. Reticular adhesions: a new class of adhesion complex that mediates cell-matrix attachment during. Nat. Cell Biol. 20, 1290–1302.
Logan, M., Rinas, K., Mcconkey, B., Aucoin, M.G., 2022. Vero cells gain renal tubule markers in low - calcium and magnesium chemically defined media. Sci. Rep. 1–13. https://doi.org/10.1038/s41598-022-10221-z.
Mao, Y., Baum, B., 2015. Tug of war — The in fl uence of opposing physical forces on epithelial cell morphology. Dev. Biol. 401, 92–102.
Meister, A., et al., 2009. FluidFM: combining atomic force microscopy and nanofluidics in a universal liquid delivery system for single cell applications and beyond. Nano Lett. 9, 2501–2507.
Mierke, C.T., 2008. Role of the endothelium during tumor cell metastasis: is the endothelium a barrier or a promoter for cell invasion and metastasis? J. Biophys. 2008, 1–13.
Mierke, C.T., 2011. Cancer cells regulate biomechanical properties of human microvascular endothelial cells. J. Biol. Chem. 286, 40025–40037.
Mierke, C.T., 2021. Bidirectional mechanical response between cells and their microenvironment. Front. Phys. 9, 1–40.
Milles, L.F., Unterauer, E.M., Nicolaus, T., Gaub, H.E., 2018. Calcium stabilizes the strongest protein fold. Nat. Commun. 9.
Nagy, A.G., et al., 2022a. Population distributions of single-cell adhesion parameters during the cell cycle from high-throughput robotic fluidic force microscopy. Sci. Rep. 12.

Nagy, A.G., Bonyar, A., Szekacs, I. & Horvath, R. Analysis of single-cell force-spectroscopy data of Vero cells recorded by FluidFM BOT. 21–25 (2020). doi: 10.1109/siitme50350.2020.9292265.
Nagy, A.G., Szekacs, I., Bonyar, A., Horvath, R., 2022b. Simple and automatic monitoring of cancer cell invasion into an epithelial monolayer using label-free holographic microscopy. Sci. Rep. 12.
Nagy, Á.G., Horvath, R., Bonyár, A. , Sztilkovics, M. A custom Software for the Evaluation of Single-Cell Force-Spectroscopy Data Acquired by FluidFM BOT. in 2021 IEEE 27th International Symposium for Design and Technology in Electronic Packaging (SIITME) (2022c). doi:10.1109/SIITME53254.2021.9663702.
Nagy, Á.G., Kámán, J., Horváth, R., Bonyár, A., 2019. Spring constant and sensitivity calibration of FluidFM micropipette cantilevers for force spectroscopy measurements. Sci. Rep. 9.
Ng, M.R. os, Besser, A., Brugge, J.S., Danuser, G., 2014. Mapping the dynamics of force transduction at cell-cell junctions of epithelial clusters. Elife 3, e03282.
Onder, T.T., et al., 2008. Loss of E-cadherin promotes metastasis via multiple downstream transcriptional pathways. Cancer Res 68, 3645–3654.
Panagiotakopoulou, M., Lendenmann, T., Michela, F., Drubin, D.G., 2018. Cell cycle – dependent force transmission in cancer cells. Mol. Biol. Cell 29, 2528–2539.
Park, E.J., Shimaoka, M., 2020. Integrin-Ligand Interactions in Inflammation, Cancer, and Metabolic Disease: Insights Into the Multifaceted Roles of an Emerging Ligand Irisin. Front. Cell Dev. Biol. 8, 1–17.
Pattison, T.G., Wang, S., Miller, R.D., Liu, G., Qiao, G.G., 2022. 3D nanoprinting via spatially controlled assembly and polymerization. Nat. Commun. 1–7. https://doi.org/10.1038/s41467-022-29432-z.
Peter, B., et al., 2015. Incubator proof miniaturized Holomonitor to in situ monitor cancer cells exposed to green tea polyphenol and preosteoblast cells adhering on nanostructured titanate surfaces: validity of the measured parameters and their corrections. J. Biomed. Opt. 20, 067002.
Potthoff, E., Ossola, D., Zambelli, T., Vorholt, J.A., 2015. Bacterial adhesion force quantification by fluidic force microscopy. Nanoscale 7, 4070–4079.
Puech, P.H., Poole, K., Knebel, D., Muller, D.J., 2006. A new technical approach to quantify cell-cell adhesion forces by AFM. Ultramicroscopy 106, 637–644.
Ricard, N., Bailly, S., Guignabert, C., Simons, M., 2021. The quiescent endothelium: signalling pathways regulating organ- specific endothelial normalcy. Nat. Rev. Cardiol. 18, 565–580.
Sader, J.E., et al., 2012. Spring constant calibration of atomic force microscope cantilevers of arbitrary shape. Rev. Sci. Instrum. 83, 103705.
Saftics, A., et al., 2019. Biomimetic dextran-based hydrogel layers for cell micropatterning over large areas using the FluidFM BOT technology. Langmuir 35, 2412–2421.
Salánki, R.U., et al., 2021. Single - cell adhesion strength and contact density drops in the M phase of cancer cells. Sci. Rep. 1–13. https://doi.org/10.1038/s41598-021-97734-1.
Sancho, A., Vandersmissen, I., Craps, S., Luttun, A., Groll, J., 2017. A new strategy to measure intercellular adhesion forces in mature cell-cell contacts. Sci. Rep. 7, 1–14.
Shen, X., et al., 2021. Extracellular Calcium Ion Concentration Regulates Chondrocyte Elastic Modulus and Adhesion Behavior. Int. J. Mol. Sci. 22.
Silverthorn, D.U., 2016. Human Physiology: An inTegrated Approach, Seventh ed.,. Pearson, USA.
Sztilkovics, M., et al., 2020. Single-cell adhesion force kinetics of cell populations from combined label-free optical biosensor and robotic fluidic force microscopy. Sci. Rep. 1–13. https://doi.org/10.1038/s41598-019-56898-7.
Tobey, N.A., Argote, C.M., Hosseini, S.S., Orlando, R.C., 2004. Calcium-switch technique and junctional permeability in native rabbit esophageal epithelium. Am. J. Physiol. Gastrointest. Liver Physiol. 286, 1042–1049.
Torras, N., García-Díaz, M., Fernández-Majada, V., Martínez, E., 2018. Mimicking epithelial tissues in three-dimensional cell culture models. Front. Bioeng. Biotechnol. 6, 1–7.
Vasquez, C.G. & Martin, A.C. 1 Vasquez, C.G. & Martin, A.C. HHS Public Access. Dev. Dyn. 245, 361–371 (2017). Dev. Dyn. 245, 361–371 (2017).
Vasquez, C.G., Vachharajani, V.T., Garzon-coral, C., Dunn, A.R., 2021. Physical basis for the determination of lumen shape in a simple epithelium. Nat. Commun. 12 (5608), 1–12.
Vianay, B., et al., 2018. Variation in traction forces during cell cycle progression. Biol. Cell 110, 91–96.
Xu, W., et al., 2012. Cell stiffness is a biomarker of the metastatic potential of ovarian cancer cells. PLoS One 7.
Zihni, C., Mills, C., Matter, K., Balda, M.S., 2016. Tight junctions: from simple barriers to multifunctional molecular gates. Nat. Rev. Mol. Cell Biol. 17, 564–580.